



OPEN ACCESS

EDITED BY

Shihua Zhong,
Ocean University of China, China

REVIEWED BY

Pf Zuo,
Henan Polytechnic University, China
Yiwei Peng,
Chengdu University of Technology,
China

*CORRESPONDENCE

Xiaobo Zhao,
✉ xiaobozhao@cugb.edu.cn

SPECIALTY SECTION

This article was submitted to Economic
Geology, a section of the journal
Frontiers in Earth Science

RECEIVED 10 February 2023

ACCEPTED 21 February 2023

PUBLISHED 09 March 2023

CITATION

Liu Y, Zhao X, Xue C, Nurtaev B and
Chen J (2023), Contrasting apatite
geochemistry between ore-bearing and
ore-barren intrusions of the giant
Kalmakyr gold-rich porphyry Cu deposit,
Tien Shan, Uzbekistan.
Front. Earth Sci. 11:1162994.
doi: 10.3389/feart.2023.1162994

COPYRIGHT

© 2023 Liu, Zhao, Xue, Nurtaev and Chen.
This is an open-access article distributed
under the terms of the [Creative
Commons Attribution License \(CC BY\)](https://creativecommons.org/licenses/by/4.0/).
The use, distribution or reproduction in
other forums is permitted, provided the
original author(s) and the copyright
owner(s) are credited and that the original
publication in this journal is cited, in
accordance with accepted academic
practice. No use, distribution or
reproduction is permitted which does not
comply with these terms.

Contrasting apatite geochemistry between ore-bearing and ore-barren intrusions of the giant Kalmakyr gold-rich porphyry Cu deposit, Tien Shan, Uzbekistan

Yangtao Liu¹, Xiaobo Zhao^{1*}, Chunji Xue^{1,2}, Bakhtiar Nurtaev³ and Jing Chen¹

¹School of Earth Sciences and Resources, China University of Geosciences, Beijing, China, ²Research Center of Resource and Environment of Xinjiang, Urumuqi, Xinjiang, China, ³Institute of Geology and Geophysics, University of Geological Sciences, State Committee of the Republic of Uzbekistan on Geology and Mineral Resources, Tashkent, Uzbekistan

The Kalmakyr deposit in Uzbekistan is one of the world's largest gold-rich porphyry Cu deposits, and mineralization was proposed to be closely associated with the emplacement of the latest intrusive phases, that is, granodiorite porphyry. However, it is still unclear which features of these ore-bearing intrusions are crucial for the enormous metal enrichment and how they correlate with magmatic fertility. In this study, we address these questions by comparing the petrological and *in situ* major and trace element geochemistry of apatite for the ore-bearing and ore-barren intrusions. Magmatic apatite from the ore-bearing granodiorite porphyry has higher Eu/Eu* (0.50–0.58), Sr/Y (1.09–1.64), and La/Yb (36.19–53.42) ratios than the ore-barren quartz porphyry (0.01–0.02, 0.02–0.03, and 2.01–3.75, respectively) and monzonite (0.20–0.11, 0.36–1.12, and 19.71–56.32, respectively). Moreover, the ore-bearing granodioritic magma has higher S (average of 111 ppm) and Cl (average of 8602 ppm) contents than the magma of quartz porphyry (S contents average of 9 ppm; Cl contents average of 2652 ppm) and monzonite (S contents average of 9 ppm; Cl contents average of 8483 ppm). These features collectively suggest that the ore-bearing granodiorite porphyry has relatively high oxygen fugacity, H₂O, Cl, and S contents compared to those from the ore-barren intrusions. By comparing our data with the published dataset from porphyry Cu–Mo and Mo-only deposits in the world, we suggest that the high Cl content and low F/Cl ratio in magmatic apatite might be an important indicator to prospect for gold-rich porphyry Cu deposits.

KEYWORDS

apatite geochemistry, oxygen fugacity, magmatic volatile contents, Kalmakyr porphyry Cu–Au deposit, Tien Shan

1 Introduction

Gold-rich porphyry Cu deposits, an essential source of gold and copper in the world, are usually associated with calc-alkaline magma, accompanied by multiphase intermediate–felsic intrusions (Sillitoe, 2010; Chiaradia, 2014; Lipson, 2014). It is noteworthy that many of these deposits appear to be related to a particular intrusive phase (Cooke et al., 2005; Chiaradia et al., 2013; Chiaradia et al., 2014; Qin et al., 2022).

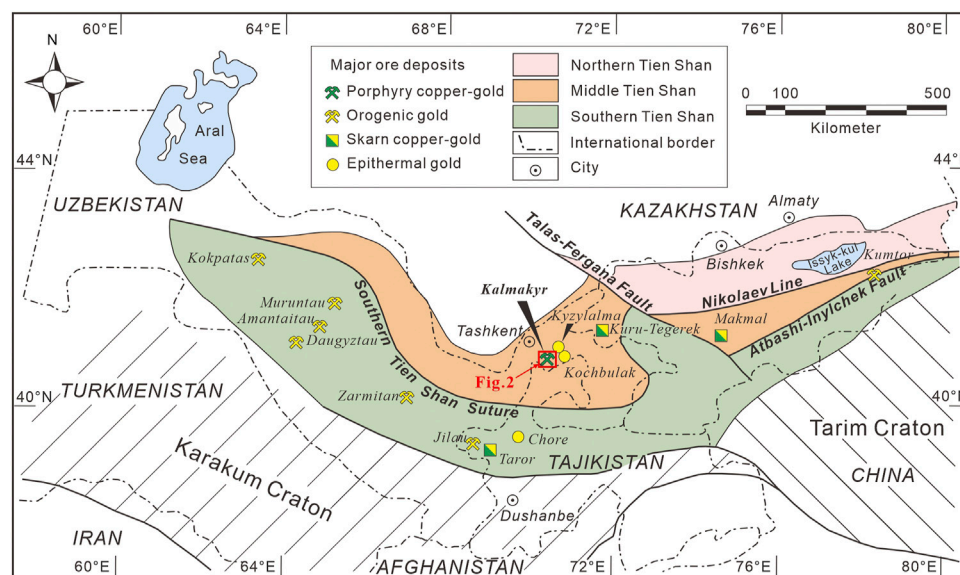


FIGURE 1

Simplified geological map of the Tien Shan orogenic belt showing the location of major copper and gold deposits (modified from (Zhao et al., 2017). The area shown in Figure 2 is marked.

Although the tectono-magmatic setting is thought to be a prerequisite for the onset of economic mineralization (Cooke et al., 2005; Sillitoe, 2010), questions as to which features of the evolving magma control mineralization potential and how they correlate with diverse metal associations are still not fully understood.

The Kalmakyr porphyry Cu-Au deposit in eastern Uzbekistan (Figure 1) has the third-largest gold endowment among all porphyry Cu deposits in the world (Cooke et al., 2005; Seltmann et al., 2014; Zhao et al., 2017). It contains measured and indicated resources of 2000 Mt of ore grading 0.4% Cu and 0.6 g/t Au (Golovanov et al., 2005). Previous studies have indicated that Cu and Au mineralization at Kalmakyr is genetically related to the latest intrusive phase, i.e., the late Carboniferous granodiorite porphyry (Golovanov et al., 2005; Zhao et al., 2017). However, the physiochemical conditions, evolution processes, and magmatic fertility of different intrusive phases at the deposit remain enigmatic and require thorough exploration. Apatite is a common accessory mineral in porphyry-associated intrusions and is resistant to physical or chemical weathering and most types of hydrothermal alteration (Sha and Chappell, 1999; Pan and Fleet, 2002; Bouzari et al., 2016; Zhong et al., 2018a; Zhong et al., 2021b). Its geochemical composition can provide diagnostic information on magma composition, physiochemical condition, evolution processes, and magmatic fertility (Bouzari et al., 2016; Chelle-Michou and Chiaradia, 2017; Xu et al., 2021).

This paper presents the results of *in situ* major and trace element geochemical analyses for apatite from the ore-barren and ore-bearing porphyry intrusions of the giant Kalmakyr porphyry Cu-Au deposit. The goal was to explore the critical features of the ore-bearing magma. These results are further integrated with available apatite geochemical data from porphyry Cu-Mo and Mo deposits to

define controlling factors that resulted in diverse metal associations in porphyry deposits.

2 Regional setting and geology of the Kalmakyr deposit

The Tien Shan orogenic belt in Uzbekistan and Kyrgyzstan comprises three suture-bounded tectonic domains, i.e., the northern, middle, and southern Tien Shan (Figure 1; Yakubchuk et al., 2002; Biske and Seltmann, 2010; Zhao et al., 2015; Zhao et al., 2022). These tectonic domains were displaced by the NW-striking Talas-Fergana strike-slip fault during the Mesozoic (Biske and Seltmann, 2010). The Kalmakyr deposit is situated within the Valerianov-Beltau-Kurama volcano-plutonic arc of the Middle Tien Shan (Figure 1; Golovanov et al., 2005). This arc is accepted to be an Andean-type arc that was formed by the northward subduction of the Turkestan Ocean during the late Paleozoic (Seltmann et al., 2011).

Porphyry Cu-Au mineralization at the Kalmakyr deposit is hosted by a late Paleozoic intrusive complex, which consists of late Devonian quartz porphyry (421 ± 4 Ma; U-Pb zircon age), middle Carboniferous monzonite (327.2 ± 5.6 Ma; U-Pb zircon age), and late Carboniferous granodiorite porphyry (313.6 ± 2.8 Ma; U-Pb zircon age; Zhao et al., 2017). The pre-mineralization quartz porphyry is exposed at the southern end of the deposit area (Figure 2). It contains phenocrysts of quartz, plagioclase, and biotite in a fine-grained quartz and feldspar groundmass (Figures 3A, D). Monzonite also undergoes pre-mineralization (Golovanov et al., 2005; Zhao et al., 2017), although it hosts most of the high-grade mineralization (Figure 2). It crops out in the central and northern sectors and gradually transitions to diorite in the western sector of the deposit area (Figure 2). Monzonite contains significant

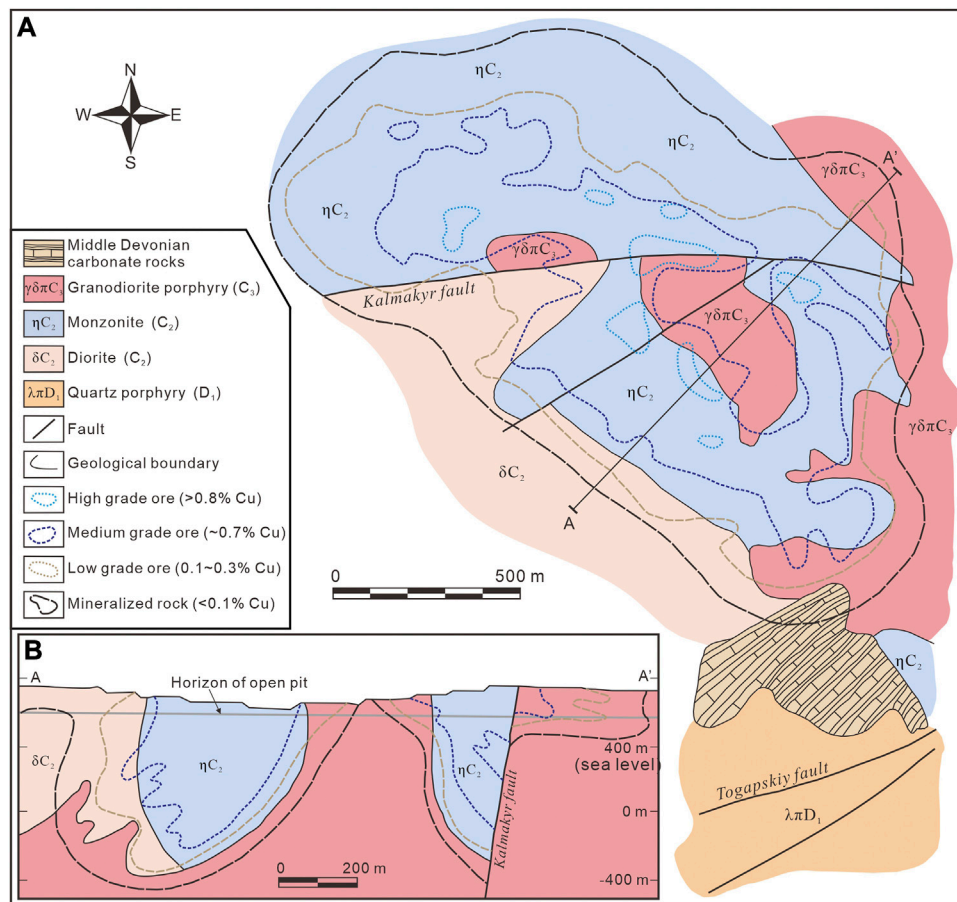


FIGURE 2 (A) Simplified geological map; and (B) Cross section of the Kalmakyr giant porphyry Cu-Au deposit [modified from (Golovanov et al., 2005) and (Zhao et al., 2017)].

amounts of coarse-grained plagioclase and K-feldspar, with minor amounts of biotite, hornblende, and quartz (Figures 3B, E). The granodiorite porphyry represents the latest intrusive phase of the deposit and is thought to be part of a larger, deep-seated intrusion with only limited exposure at the surface (Golovanov et al., 2005). This unit comprises phenocrysts of plagioclase, quartz, K-feldspar, hornblende, and biotite within a felsic groundmass (Figures 3C, F).

Hydrothermal alteration and Cu-Au mineralization occur widely in the deposit area and are associated with the emplacement of the granodiorite porphyry (Golovanov et al., 2005; Zhao et al., 2017). Upward and outward from the barren core of granodiorite porphyry, hydrothermal alteration shows zonation from early K-silicate to the ore-hosting phyllic zone and later the propylitic zone (Golovanov et al., 2005). The phyllic alteration contains the quartz-sericite and quartz-sericite-chlorite-biotite zones, with extensive Cu and Au mineralization and high-grade ores spatially related to the latter zone (Golovanov et al., 2005; Turamuratov et al., 2011). Mineralization is characterized by stockwork and veinlets of chalcopyrite, pyrite, and molybdenite, as is common in many gold-rich porphyry Cu deposits (Sillitoe, 2010; Li et al., 2022; Yang et al., 2022; Tang et al., 2023).

3 Sampling and analytical methods

Intrusive samples with limited alteration were collected from outcrops around the Kalmakyr open pit for apatite geochemical analyses. The granodiorite porphyry (samples KM-2, KM-3, KM-4, and KM-6) is regarded as ore-bearing, whereas quartz porphyry (sample KM-12) and monzonite (samples KM-24, KM-25, and KM-26) represent ore-barren intrusions. All samples were polished to 100- μm -thick and -thin sections for petrological and *in situ* geochemical analyses, respectively. Apatite grains were selected by optical and backscattered electron (BSE) microscopy. Major and trace element geochemistry of apatite grains were analyzed *in situ* by electron microprobe (EMP) analyses and laser ablation inductively coupled plasma mass spectrometry (LA-ICP-MS), respectively.

A JEOL-JXA8100 electron microprobe performed BSE imaging and the EMP analyses of apatite with a 15-kV accelerating voltage, 10-nA beam current, and 3- μm probe beam at the MNR Key Laboratory of Metallogeny and Mineral Assessment, Institute of Mineral Resources, Chinese Academy of Geological Sciences, Beijing. To detect the characteristic X-ray patterns, 20 s of counting time was chosen for Si, Al, Ti, Fe, Mn, K, Na, Ba, Cl, and S, 40 s for F, and 10 s for Ca and P. Trace element contents in apatite were analyzed by LA-ICP-MS at the

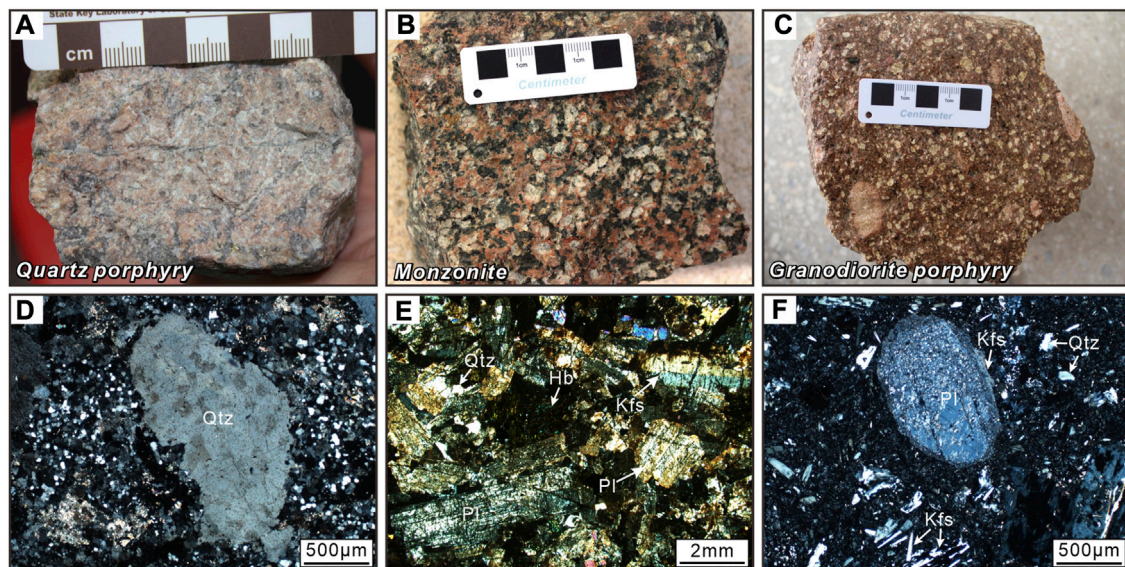


FIGURE 3

Photographs and photomicrographs showing the main texture and mineral assemblages of three major intrusions of the Kalmayr deposit. (A) Quartz porphyry; (B) Monzonite; (C) Granodiorite porphyry; (D) Anhedra quartz phenocrysts of quartz porphyry under cross-polarized light; (E) Euhedral to subhedral, plagioclase, and K-feldspar, and minor biotite, hornblende, and quartz phenocrysts in monzonite under cross-polarized light; (F) Plagioclase phenocryst partially rimmed by K-feldspar in granodiorite porphyry under cross-polarized light. Mineral abbreviations: Qtz, quartz; Pl, plagioclase; Kfs, K-feldspar; Hb, hornblende; Bio, biotite.

Ore Deposit and Exploration Centre, Hefei University of Technology. The analyses consist of an Agilent 7900 ICP-MS instrument and a Cetac Analyte HE laser ablation system with helium (0.9 L min^{-1}) as the carrier gas and argon (0.87 L min^{-1}) as the compensation gas to enhance the sensitivity, and they mixed via a T-connector before entering the ICP. After testing the gas blank for 20 s, the laser was run for 40 s at a constant repetition rate of 7 Hz with an energy density of 4 J cm^{-2} and a beam aperture of $30 \mu\text{m}$. NIST 610, NIST 612, and BCR 2G, as the external standards, were run after every 10 analyses. Measured by EMP analyses, the Ca concentrations were used as the internal standards for apatite. The detection limits were calculated for each element in each spot analysis. The analysis accuracy of most trace elements is greater than 10%. The data reduction and processing were carried out using ICPMSDataCal software (Liu et al., 2008).

4 Results

4.1 Apatite petrography

Typical microscopic and BSE images of apatite from quartz porphyry, monzonite, and granodiorite porphyry of the Kalmayr deposit are presented in Figure 4. Apatite grains from quartz porphyry are euhedral to subhedral columnar crystals of $50\text{--}200 \mu\text{m}$ in length, occurring mostly as inclusions in biotite phenocryst (Figures 4A, B). The majority of these apatite grains display a homogenous texture with a weak core-rim texture and few gaps or cracks in the BSE images (Figures 4B, C). Apatite crystals from the monzonite are euhedral to subhedral, with prismatic and granular crystals of $25\text{--}120 \mu\text{m}$ in size (Figures 4D, E). They occur as inclusions in plagioclase and hornblende, and some are also

dispersed in the groundmass (Figures 4D, E). In BSE images, some apatite grains have a homogeneous texture, and some of the apatite grains have mineral or fluid inclusions (Figures 4E, F). Apatite grains from the granodiorite porphyry are euhedral to subhedral columnar and granular crystals of $20\text{--}70 \mu\text{m}$ in size, which are commonly wrapped by plagioclase and biotite (Figures 4G, H). These apatite grains show a homogeneous texture with an inclusion-free surface (Figures 4H, I).

4.2 Apatite major and trace element composition

Apatite major and trace element compositions from the ore-bearing and ore-barren intrusions of the Kalmayr deposit are summarized in Supplementary Table S1. A total of 27 apatite grains, including 7 grains for granodiorite porphyry, 6 grains for quartz porphyry, and 14 grains for monzonite, were selected for EMP analyses and LA-ICP-MS in this study.

Apatite grains from the granodiorite porphyry, quartz porphyry, and monzonite have similar CaO ($53.74\text{--}55.48 \text{ wt}\%$, $52.05\text{--}54.46 \text{ wt}\%$, and $53.46\text{--}55.28 \text{ wt}\%$, respectively), P_2O_5 ($39.99\text{--}41.31 \text{ wt}\%$, $40.55\text{--}41.56 \text{ wt}\%$, and $39.56\text{--}41.94 \text{ wt}\%$, respectively), Na_2O ($0\text{--}0.016 \text{ wt}\%$, $0.25\text{--}0.35 \text{ wt}\%$, and $0\text{--}0.16 \text{ wt}\%$, respectively), and MnO contents ($0.11\text{--}0.17 \text{ wt}\%$, $0.12\text{--}0.22 \text{ wt}\%$, and $0\text{--}0.18 \text{ wt}\%$, respectively). The K_2O contents are usually close to or below their detection limits. According to the SiO_2 and MnO contents, most apatite grains are plotted in the magmatic apatite field in the SiO_2 vs. MnO diagram (Chen and Zhang, 2018; Figure 5A). The negative correlation of MnO and CaO indicates the equivalent substitution of Ca^{2+} by Mn^{2+}

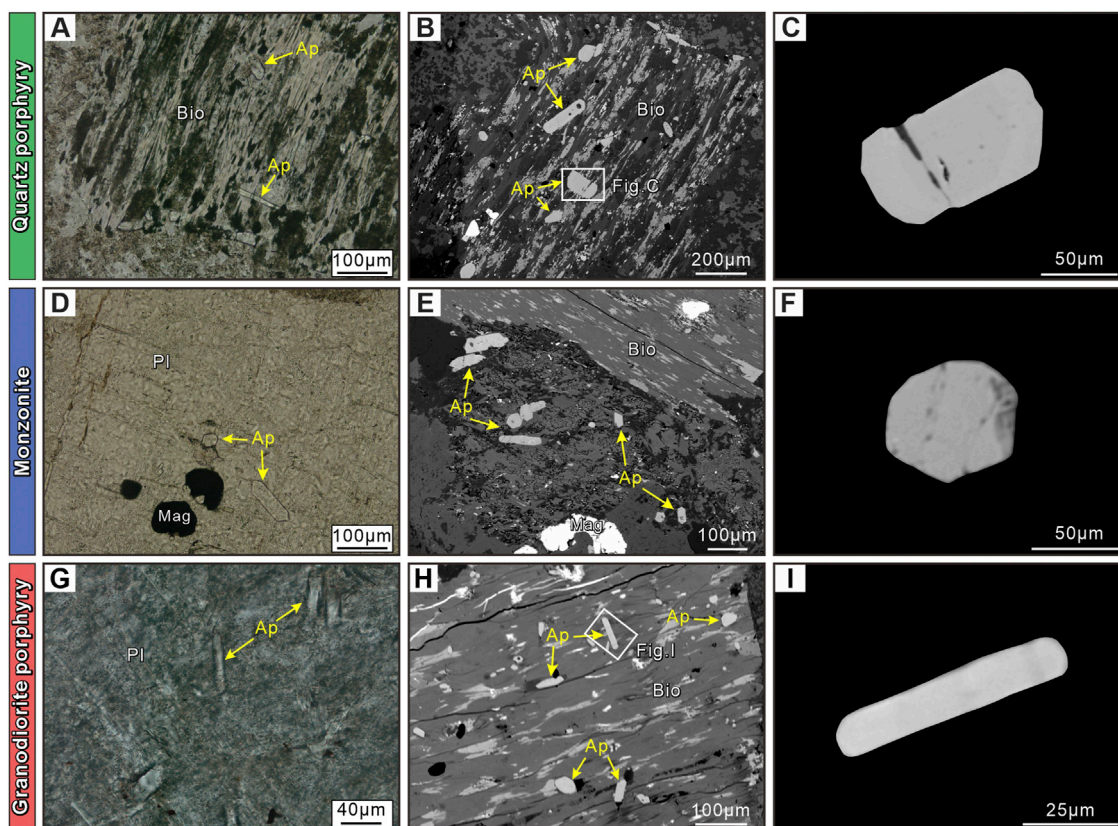
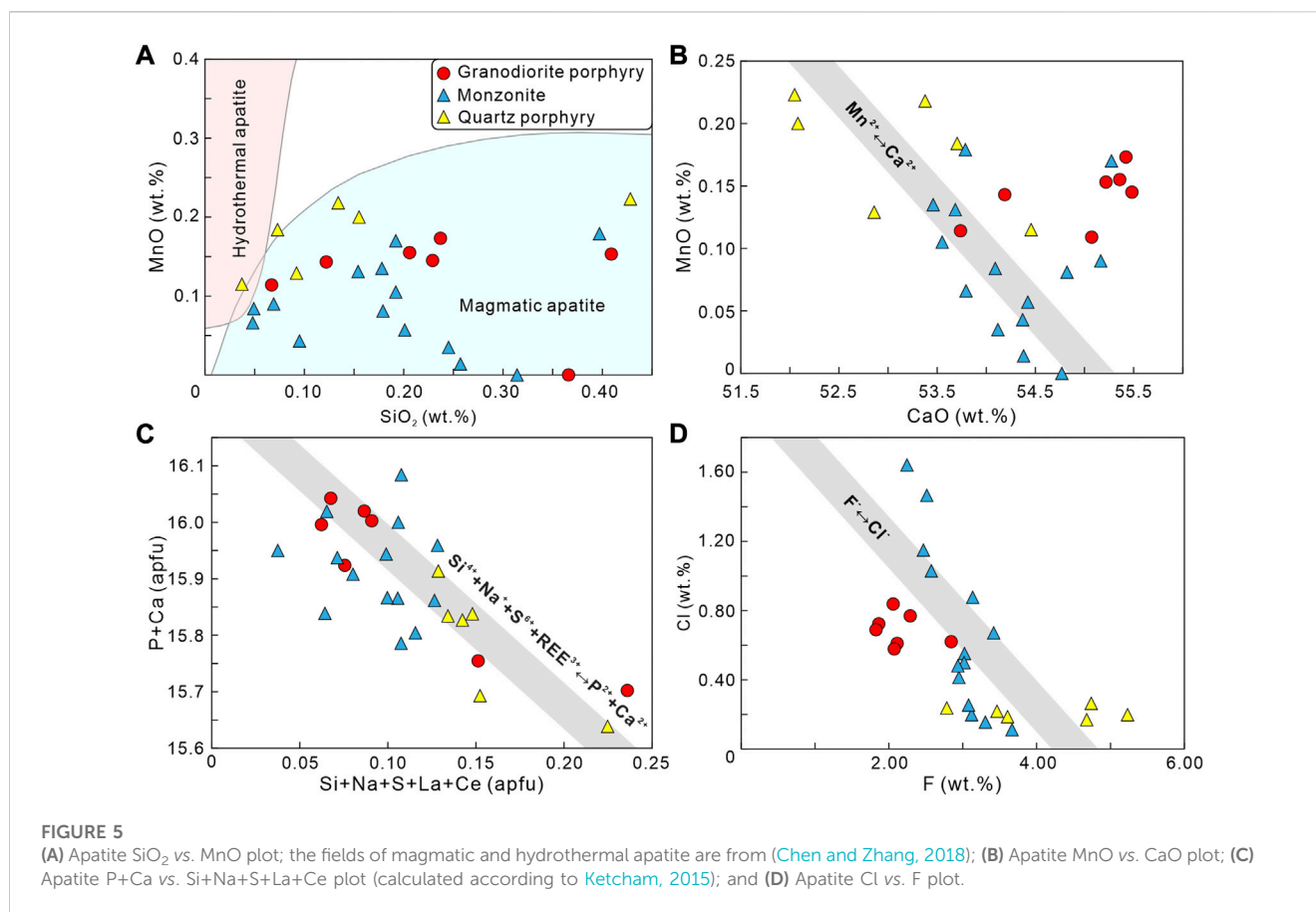


FIGURE 4

Plane-polarized photomicrographs (A, D, G) and BSE images (B, C, E, F, H, I) illustrating petrographic features of representative apatite from the Kalmakyr porphyry deposit. (A) Euhedral to subhedral, elongated and columnar magmatic apatite occurs as inclusions in quartz porphyry's biotite; (B) Euhedral to subhedral, homogeneous magmatic apatite occurs as inclusions in quartz porphyry's biotite; (C) Unaltered magmatic apatite, displaying a weak core–rim texture and the homogeneous surface of quartz porphyry; (D) Euhedral to subhedral, prismatic and granular magmatic apatite occurs as inclusions in the plagioclase phenocryst of monzonite; (E) Euhedral to subhedral magmatic apatite with minor mineral inclusions of monzonite; (F) Granular magmatic apatite of monzonite; (G) Euhedral to subhedral, columnar magmatic apatite occurs as inclusions in the plagioclase phenocryst of granodiorite porphyry; (H) Euhedral to subhedral, columnar and granular magmatic apatite occurs as inclusions in the biotite phenocryst of granodiorite porphyry; and (I) Columnar magmatic apatite with a homogeneous surface of granodiorite porphyry. Mineral abbreviations: Ap, apatite; Bio, biotite; Pl, plagioclase; Mag, magnetite.

(Pan and Fleet, 2002; Figure 5B). Ca and P show a negative correlation with Si, S, Na, La, and Ce (Figure 5C), which indicates the following substitutions: $\text{Na}^+ + \text{S}^{6+} = \text{Ca}^{2+} + \text{P}^{5+}$, $\text{REE}^{3+} + \text{Si}^{4+} = \text{Ca}^{2+} + \text{P}^{5+}$, $\text{REE}^{3+} + \text{Na}^+ = 2\text{Ca}^{2+}$, and $\text{S}^{6+} + \text{Si}^{4+} = 2\text{P}^{5+}$ (Sha and Chappell, 1999; Mao et al., 2016). All apatite grains have higher F contents than Cl, indicating that they are fluorapatite. The negative correlation between Cl and F supports the reciprocal substitution of Cl^- and F^- (Pan and Fleet, 2002; Figure 5D). Apatite grains from the granodiorite porphyry have higher Cl contents (average of 0.69 wt%, $n=7$) and lower F contents (average of 2.15 wt%, $n=7$) compared with those from quartz porphyry, i.e., Cl (average of 0.21 wt%, $n=6$) and F (average of 4.08 wt%, $n=6$), but are comparable to those from monzonite (average Cl content of 0.68 wt%, $n=14$, and average F content of 2.96 wt%, $n=14$). In addition, apatite in the granodiorite porphyry has higher SO_3 concentrations (average of 0.19 wt%, $n=7$) compared with those from the quartz porphyry (average of 0.02 wt%, $n=6$) and monzonite (average of 0.03 wt%, $n=14$).

Chondrite-normalized rare earth element (REE) patterns of apatite grains from the three intrusive phases all show enrichment of light REE and depletion of heavy REE, with weak positive Ce anomalies and variably negative Eu anomalies (Figure 6). The total REE contents of apatite from granodiorite porphyry (3929–7428 ppm, average of 4926 ppm) are lower than those from quartz porphyry (9532–13260 ppm, average of 11073 ppm) and monzonite (3032–10199 ppm, average of 6546 ppm). Eu/Eu^* of apatite from granodiorite porphyry (average of 0.53) is higher than that from quartz porphyry (average of 0.01) and monzonite (average of 0.14; Figure 7). Meanwhile, the apatite grains from granodiorite porphyry have Sr contents of 328.83–734.07 ppm (average of 476.07 ppm) and Y contents of 258.85–446.30 ppm (average of 345.47 ppm), with a Sr/Y ratio of 1.09–1.64. Comparatively, the apatite grains from quartz porphyry and monzonite have lower Sr contents (93.97–131.06, and 217.45–417.40 ppm, respectively), higher Y contents (4858.77–7200.35, and 342.67–705.78 ppm, respectively), and a lower Sr/Y ratio (0.01–0.03, 0.36–1.12, respectively; Figures 7, 8).



5 Discussion

5.1 Origin of apatite in multiphase intrusions

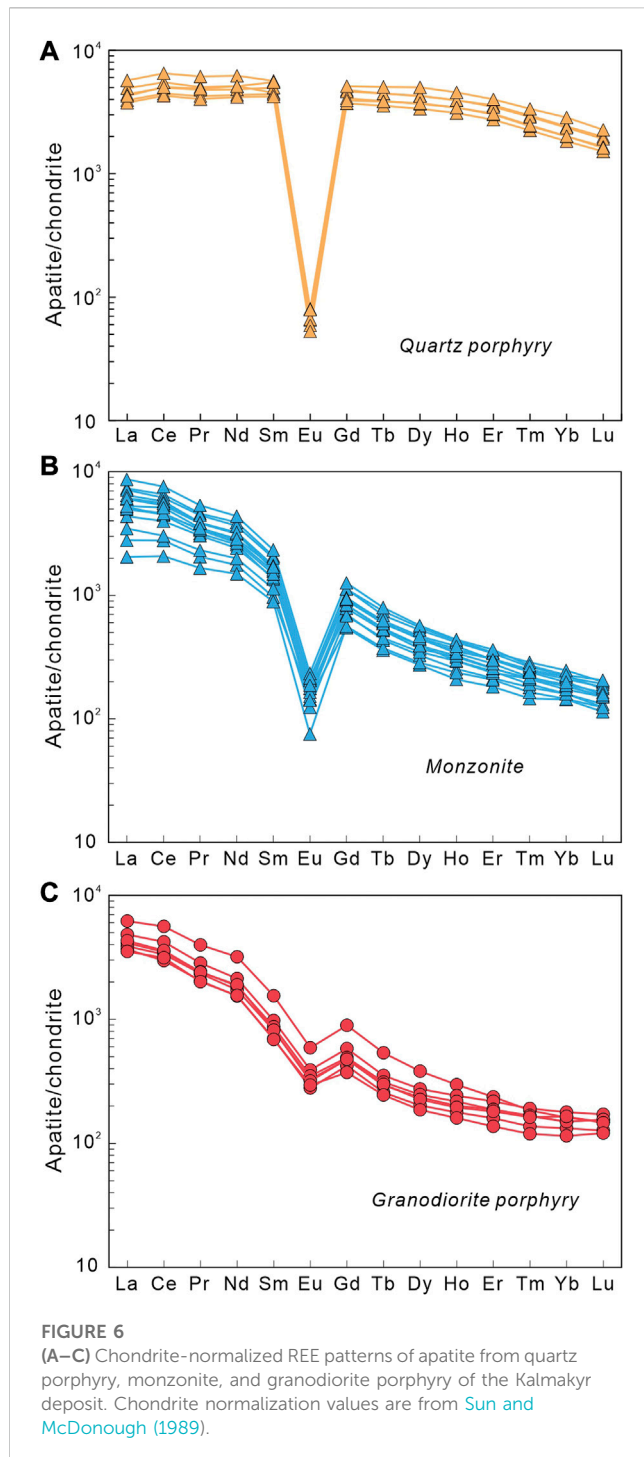
Magmatic apatite is generally formed in the early stages of the evolving magma, while hydrothermal apatite appears to be formed during the magmatic–hydrothermal transition or later hydrothermal stages (Bouzari et al., 2016). However, only those magmatic apatite crystals without alteration overprinting can provide original information on the parental magma (Xing et al., 2020; Pan et al., 2021; Xing et al., 2021). Most of the analyzed apatite grains from the three intrusive phases are hosted by biotite, hornblende, and plagioclase phenocrysts (Figure 4). BSE images show that the majority of apatite grains are homogeneous, and only some apatite grains from monzonite contain mineral or fluid inclusions (Figure 4E). These grains are ignored during our *in situ* geochemical analyses. In this study, almost all apatite grains are plotted in the magmatic apatite field in the SiO₂ vs. MnO diagram (Chen and Zhang, 2018; Figure 5A). Moreover, the Cl contents of all analyzed apatite grains (<1.64 wt %) are significantly lower than those of hydrothermal apatite (usually exceeding 3.0 wt%; Palma et al., 2019). The apatite grains for a single intrusive phase show parallel REE patterns (Figure 6). It is, therefore, indicated that the analyzed apatite crystals from all three intrusive phases are magmatic apatite and can document

the initial information on their parental magma. Although these apatite grains are magmatic, there are subtle differences in the apatite of the three intrusions. In petrography, apatite crystals from granodiorite porphyry are more fine-grained and homogeneous on the surface compared to those from quartz porphyry and monzonite (Figure 4).

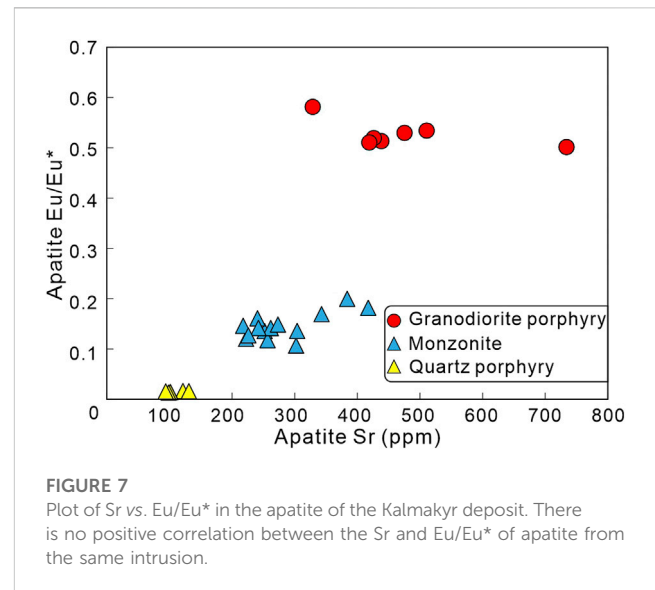
5.2 Magmatic oxidation state and compositions of multiphase magma

5.2.1 Magmatic oxidation state

Oxidized magma has a higher ability to convey metals and sulfur from the mantle to the shallow crust because sulfur in oxidized magma mainly exists as sulfate (SO₄²⁻) that is incompatible with chalcophile elements (Jugo, 2009; Richards, 2011; Zhong et al., 2018b; Zhong et al., 2019; Zhong et al., 2021c). The apatite Eu/Eu* value is an important indicator of magmatic oxygen fugacity since Eu³⁺ has a similar ionic radius with Ca²⁺ and is easier to substitute Ca²⁺ in the apatite lattice than Eu²⁺, which will result in high apatite Eu/Eu* values in the more oxidized magma (Sha and Chappell, 1999; Piccoli and Candela, 2002). At the Kalmakyr deposit, all the analyzed apatite grains show negative Eu/Eu* anomalies (Figure 8A). However, it should be noted that the Eu/Eu* values of apatite from the granodiorite porphyry (0.50–0.58,



average of 0.53) are higher than those from the quartz porphyry (0.01–0.02, average of 0.01) and monzonite (0.20–0.11, average of 0.14) but are identical to ore-bearing intrusions from porphyry deposits elsewhere (Figure 8A). This indicates that the granodiorite magma may be more oxidized than the quartz porphyry and monzonitic magma. This inference is supported by the relatively high Ce^{4+}/Ce^{3+} values (average 890) for zircon grains from the granodiorite porphyry (Zhao et al., 2017). Feldspar crystallization may also lead to negative Eu anomalies, accompanied by a significant reduction in Sr contents in the coexisting melt (Pan



et al., 2021). There is no apparent positive correlation between apatite Eu/Eu* and Sr from a single intrusive phase, which excludes the previous conjecture (Figure 7). Therefore, the negative Eu anomalies are more likely to be caused by magma in an oxidized state. However, apatite grains from ore-bearing and ore-barren intrusions display similar Ce/Ce* (weakly positive; Figure 8A), indicating that apatite Ce/Ce* does not have a relationship with magmatic oxygen fugacity (Zhong et al., 2018a; Xing et al., 2021).

5.2.2 Magmatic H₂O content

A high H₂O content in oxidized magma is necessary for the exsolution of an aqueous volatile phase to release copper and gold (Richards, 2011; Lu et al., 2015; Zhong et al., 2021a). Magma with high H₂O contents favors hornblende and garnet crystallization in early deep crust fractionation and would suppress plagioclase crystallization, resulting in elevated Sr/Y and La/Yb ratios (Richards, 2011; Nathwani et al., 2020). Many studies have shown that the characteristics of high Sr/Y and La/Yb in the hydrous magma can be recorded by the early crystallization of apatite (Nathwani et al., 2020; Xing et al., 2021). Petrographic observation indicates that apatite in all three intrusive phases occurs dominantly as an inclusion in phenocrysts such as biotite, plagioclase, and hornblende (Figure 4), suggesting that they may have been formed during the early stage of the evolving magma. The apatite in granodiorite porphyry shows relatively high Sr/Y ratios (1.09–1.64) and La/Yb ratios (36.19–53.42). This characteristic resembles ore-bearing intrusions from many other porphyry Cu–Au±(Mo) deposits (Pan et al., 2016; Qu et al., 2021) but it is obviously higher than those of quartz porphyry (Sr/Y = 0.02–0.03; La/Yb = 2.01–3.75) and other ore-barren intrusions (Qu et al., 2019; Figure 8B). This indicates that the H₂O content of the granodiorite porphyry is higher than that of the ore-barren quartz porphyry. Although the apatite from the monzonite intrusion has roughly similar Sr/Y (0.36–1.12) and La/Dy (19.71–56.32) ratios to those from granodiorite porphyry (Figure 8B), the apatite from the

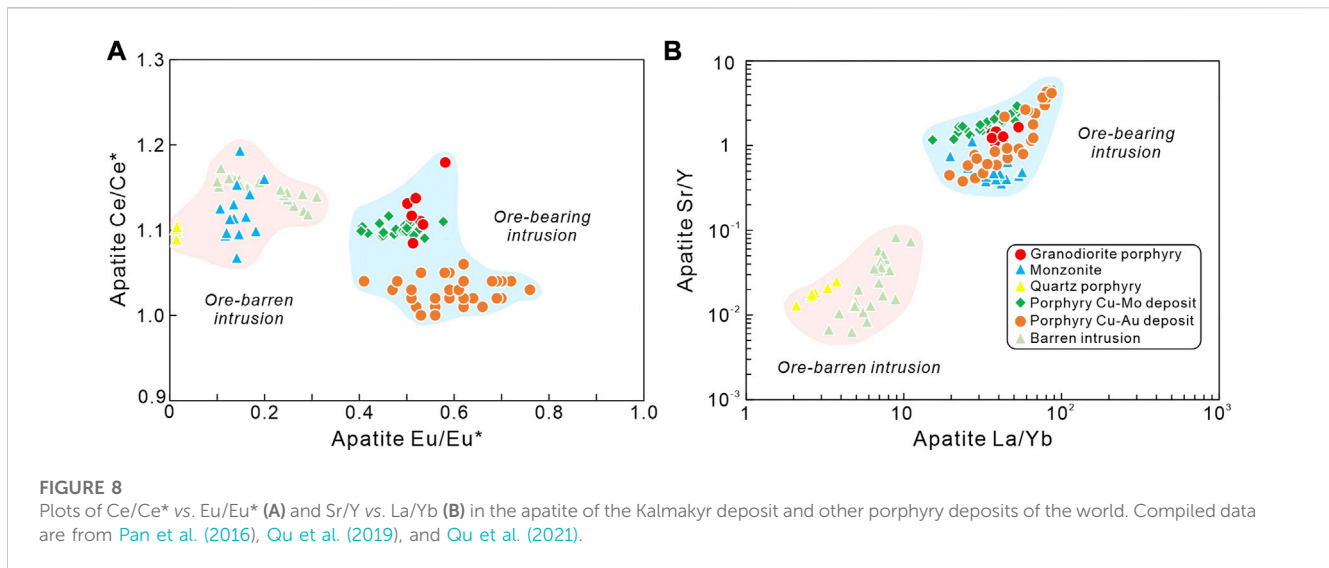


TABLE 1 Estimated S, Cl, and F contents in the porphyry-associated magma of the Kalmakyr deposit using apatite geochemical compositions.

Intrusion	Average apatite SO ₃ content	Average apatite F content	Average apatite Cl content	Average magmatic S content ^a	Average magmatic F content ^b	Average magmatic Cl content ^b
	wt%	wt%	wt%	ppm	ppm	ppm
Quartz porphyry	0.02	4.08	0.21	9	12010	2652
Monzonite	0.03	2.96	0.68	9	8706	8483
Granodiorite porphyry	0.19	2.15	0.69	111	6329	8620

^aMethod developed by Parat et al. (2011).

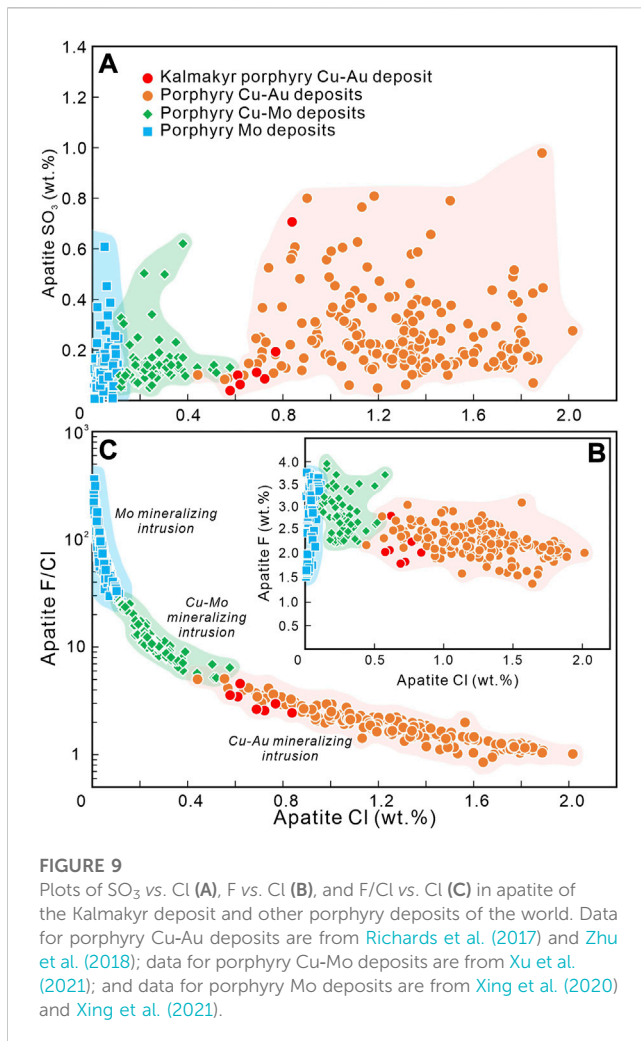
^bMethod developed by Mathez and Webster, 2005.

monzonite intrusion shows relatively lower Sr/Y and La/Dy ratios. Moreover, zircon grains in granodiorite porphyry exhibit higher ($10000 \times \text{Eu}/\text{Eu}^*$)/Y ratios (5.33–24.49) and lower Dy/Yb ratios (0.12–0.21) than those from the monzonite intrusion, that is, $(10000 \times \text{Eu}/\text{Eu}^*)/Y = 1.53\text{--}7.23$, and $\text{Dy}/\text{Yb} = 0.19\text{--}0.44$ (Zhao et al., 2017). It is, therefore, concluded that the magma of granodiorite porphyry has a higher H₂O content than the magma of monzonite and quartz porphyry (Lu et al., 2016; Zhu et al., 2018).

5.2.3 Magmatic F, S, and Cl contents

Magmatic volatile compositions play a critical role in porphyry mineralization, largely due to the fact that they can form chemical ligands with metals (Cu and Au) that are favorable for migration and metal enrichment (Piccoli and Candela, 2002; Yardley, 2005; Jugo, 2009; Zhong et al., 2018a). According to many past studies, apatite wrapped in other igneous minerals as inclusions can preserve the initial volatile content of magma (Stock et al., 2016; Zhu et al., 2018; Li et al., 2021; Pan et al., 2021; Zhu et al., 2022). As we have previously discussed, most of the analyzed apatite grains fit this feature and could theoretically record the original volatile content of the magma. The Cl and F contents of parental magma for the three intrusive phases were

calculated according to the apatite/melt partition coefficients proposed by Mathez and Webster (2005), whereas the S abundance in the parental magma was calculated according to the apatite/melt partition coefficients proposed by Parat et al. (2011). The results (Table 1) show that the Cl contents of granodioritic magma (average of 8602 ppm) are significantly higher than the magma of quartz porphyry (average of 2652 ppm) but are consistent with the monzonitic magma (average of 8483 ppm). We, therefore, infer that the Cl-rich hydrothermal fluids exsolved from the ore-bearing granodiorite porphyry may have altered the Cl content of apatite from ore-barren monzonite. The Cl-rich hydrothermal fluids not only affect the apatite Cl content but are also capable of carrying or extracting metals from the monzonite intrusion (Zajacz et al., 2012). For the F content, it is generally recognized that F is partitioned more difficultly into aqueous fluids relative to Cl (Stock et al., 2016; Li et al., 2021); thus, the F content of apatite is basically not altered by the late hydrothermal fluids. The F contents of granodioritic magma (average of 6329 ppm) are lower than those of the magmas for quartz porphyry (average of 12010 ppm) and monzonite (average of 8706 ppm), which indicate that F, unlike Cl, possibly has little influence on the extraction and transport of Cu and Au during the magmatic-hydrothermal evolution. Furthermore, the S



contents of granodioritic magma (average of 111 ppm) are higher than those of magma for quartz porphyry (average of 9 ppm) and monzonite (average of 9 ppm). This result is also supported by the development of numerous anhydrite veins in the mineralized zones since anhydrite is an indicator of sulfur-rich and oxidized melts (Golovanov et al., 2005; Zhao et al., 2017; Hutchinson and Dilles, 2019; Li et al., 2021). To summarize, we conclude that the ore-bearing granodioritic magma is characterized by being Cl- and S-rich, and F-poor compared with the magma for the ore-barren quartz porphyry and monzonite.

5.3 Exploration indication for gold-rich porphyry deposits

The porphyry deposit contains significant resources of Cu, Mo, and Au, forming different subgroups with diverse metal associations (e.g., Cu-Au, Cu-Mo, and Mo; Sillitoe, 2010). Magmatic volatile (F, Cl, and S) contents have been proposed to be an important controlling factor for their difference (Zajacz et al., 2012); however, which magmatic features are most critical remains unclear. In this study, we attempted to address this question by comparing the volatile contents of apatite from the ore-bearing

granodiorite porphyry at Kalmakyr with available data from porphyry Cu-Au, Cu-Mo, and Mo deposits around the world. As shown in Figures 9A, B, the apatite SO_3 and F contents for ore-bearing intrusions in porphyry Cu-Au, Cu-Mo, and Mo-only deposits are essentially similar, suggesting that these contents in magma may not be key factors controlling metal differences. In contrast, the Cl content and F/Cl ratio in apatite vary significantly (Figure 9C), i.e., gold-rich porphyry deposits contain the highest Cl content (0.4–2.0 wt%) with the lowest F/Cl ratio (0.8–8.0), Cu-Mo porphyry deposits have a moderate Cl content (0.1–0.6 wt%) and F/Cl ratio (5.0–30), and Mo-only porphyry deposits show the lowest Cl content (0.01–0.12 wt%) with the highest F/Cl ratio (25–360). This variation might be related to the higher solubility of Au relative to Cu and Mo in Cl-rich melts, resulting in elevated Au enrichment in evolving magma (Zajacz et al., 2012). It is, therefore, suggested that the Cl content in evolving magma might be one of the crucial factors controlling the diverse metal associations in porphyry deposits, and a high apatite Cl content (0.4–2.0 wt%) and low F/Cl ratio (0.8–8.0) in ore-bearing intrusions could be used as an important exploration indicator for gold-rich porphyry Cu deposits.

6 Conclusion

- 1) Apatite in multiphase intrusions occurs as inclusions within early phenocrysts, with a homogeneous surface and low Cl and moderate SiO_2 contents, indicating a magmatic origin.
- 2) The ore-bearing granodiorite porphyry at Kalmakyr is characterized by high oxygen fugacity and high H_2O , Cl, and S contents compared to the ore-barren intrusions.
- 3) A high Cl content (0.4–2.0 wt%) and low F/Cl ratio (0.8–8.0) in magmatic apatite can be used as an important indicator to prospect gold-rich porphyry Cu deposits.

Data availability statement

The original contributions presented in the study are included in the article/Supplementary Material, further inquiries can be directed to the corresponding author.

Author contributions

YL: investigation, analysis of the data, methodology, and writing—original draft. XZ: investigation, conceptualization, sample collection, designing the experiment, supervision, and writing—review and editing. CX: investigation, supervision, and writing—review and editing. BN: investigation and writing—review and editing. JC: conducting the experiment.

Funding

The authors declare that this study received funding from Zijin Mining Group Co., Ltd. The funder was not involved in the study design, collection, analysis, interpretation of data, the writing of this article, or the decision to submit it for publication.

This study was sponsored by the National Natural Science Foundation of China (U1303292, 42202100), the Open Research projects from the State Key Laboratory of Geological Processes and Mineral Resources (GPMR202117) of Beijing, China, and the MNR Key Laboratory of Metallogeny and Mineral Assessment (ZS2204) of Beijing, China, and Zijin Mining Group Co., Ltd.

CX acknowledges funding under Department of Human Resources and Social Security of Xinjiang Uygur Autonomous Region Introduced Project “Tianchi talent”.

Acknowledgments

The authors are grateful to Fangyue Wang and Xiaohong Mao for their help during the analysis. This paper benefits from thoughtful reviews by reviewers and editorial handling by Shihua Zhong.

Conflict of interest

The authors declare that the research was conducted in the absence of any commercial or financial relationships that could be construed as a potential conflict of interest.

References

- Biske, Y. S., and Seltmann, R. (2010). Paleozoic tian-shan as a transitional region between the rheic and urals-turkestan oceans. *Gondwana Res.* 17 (2-3), 602–613. doi:10.1016/j.gr.2009.11.014
- Bouzar, F., Hart, C. J., Bissig, T., and Barker, S. (2016). Hydrothermal alteration revealed by apatite luminescence and chemistry: A potential indicator mineral for exploring covered porphyry copper deposits. *Econ. Geol.* 111 (6), 1397–1410. doi:10.2113/econgeo.111.6.1397
- Chelle-Michou, C., and Chiaradia, M. (2017). Amphibole and apatite insights into the evolution and mass balance of Cl and S in magmas associated with porphyry copper deposits. *Contributions Mineralogy Petrology* 172 (11-12), 105. doi:10.1007/s00410-017-1417-2
- Chen, L., and Zhang, Y. (2018). *In situ* major-trace-elements and Sr-Nd isotopic compositions of apatite from the Luming porphyry Mo deposit, NE China: Constraints on the petrogenetic-metallogenic features. *Ore Geol. Rev.* 94, 93–103. doi:10.1016/j.oregeorev.2018.01.026
- Chiaradia, M. (2014). Copper enrichment in arc magmas controlled by overriding plate thickness. *Nat. Geosci.* 7 (1), 43–46. doi:10.1038/ngeo2028
- Chiaradia, M., Schaltegger, U., and Spikings, R. (2014). Time scales of mineral systems—Advances in understanding over the past decade. *Soc. Econ. Geol. -Special Publ.* 18, 37–58. doi:10.5382/SP.18.03
- Chiaradia, M., Schaltegger, U., Spikings, R., Wotzlav, J. F., and Ovtcharova, M. (2013). How accurately can we date the duration of magmatic-hydrothermal events in porphyry systems? —an invited paper. *Econ. Geol.* 108 (4), 565–584. doi:10.2113/econgeo.108.4.565
- Cooke, D. R., Hollings, P., and Walshe, J. L. (2005). Giant porphyry deposits: Characteristics, distribution, and tectonic controls. *Econ. Geol.* 100 (5), 801–818. doi:10.2113/gsecongeo.100.5.801
- Golovanov, I. M., Seltmann, R., Kremenetsky, A. A., and Porter, T. (2005). “The almalayk (Kalmakyr–Dalnee) and saukbulak Cu–Au porphyry systems, Uzbekistan,” in *Super porphyry copper and gold deposits: A global perspective*, 2. Editor T. M. Porter (Adelaide: PGC Publishing), The porphyry Cu–Au/Mo deposits of Central Euroasia, 2, 513–523.
- Hutchinson, M. C., and Dilles, J. H. (2019). Evidence for magmatic anhydrite in porphyry copper intrusions. *Econ. Geol.* 114 (1), 143–152. doi:10.5382/econgeo.2019.4624
- Jugo, P. J. (2009). Sulfur content at sulfide saturation in oxidized magmas. *Geology* 37(5), 415–418. doi:10.1130/g25527a.1
- Ketcham, R. A. (2015). Technical Note: Calculation of stoichiometry from EMP data for apatite and other phases with mixing on monovalent anion sites. *Am. Mineralogist* 100 (7), 1620–1623. doi:10.2138/am-2015-5171
- Li, J. X., Li, G. M., Evans, N. J., Zhao, J. X., Qin, K. Z., and Xie, J. (2021). Primary fluid exsolution in porphyry copper systems: Evidence from magmatic apatite and anhydrite inclusions in zircon. *Miner. Deposita* 56, 407–415. doi:10.1007/s00126-020-01013-4
- Li, W. C., Zhang, X. F., Yu, H. J., Tao, D., and Liu, X. L. (2022). Geology and mineralization of the pulang supergiant porphyry copper deposit (5.11 Mt) in shangri-la, yunnan province, China: A review. *China Geol.* 5 (4), 662–695.
- Lipson, R. (2014). The promise and perils of porphyry deposits in the future of gold production. *Seg. Discov.* 98, 1–21. doi:10.5382/segnews.2014.98.fea
- Liu, Y., Hu, Z., Gao, S., Günther, D., Xu, J., Gao, C., et al. (2008). *In situ* analysis of major and trace elements of anhydrous minerals by LA-ICP-MS without applying an internal standard. *Chem. Geol.* 257 (1-2), 34–43. doi:10.1016/j.chemgeo.2008.08.004
- Lu, Y. J., Loucks, R. R., Fiorentini, M. L., Yang, Z. M., and Hou, Z. Q. (2015). Fluid flux melting generated postcollisional high Sr/Y copper ore-forming water-rich magmas in Tibet. *Geology*, 43(7), 583–586. doi:10.1130/g36734.1
- Lu, Y. J., Loucks, R. R., Fiorentini, M., McCuaig, T. C., Evans, N. J., Yang, Z. M., et al. (2016). Zircon compositions as a pathfinder for porphyry Cu±Mo±Au deposits. *Soc. Econ. Geol. -Special Publ.* 19, 1–57. doi:10.5382/SP.19.13
- Mao, M., Rukhlov, A. S., Rowins, S. M., Spence, J., and Coogan, L. A. (2016). Apatite trace element compositions: A robust new tool for mineral exploration. *Econ. Geol.* 111 (5), 1187–1222. doi:10.2113/econgeo.111.5.1187
- Mathez, E. A., and Webster, J. D. (2005). Partitioning behavior of chlorine and fluorine in the system apatite-silicate melt-fluid. *Geochimica Cosmochimica Acta* 69 (5), 1275–1286. doi:10.1016/j.gca.2004.08.035
- Nathwani, C. L., Loader, M. A., Wilkinson, J. J., Buret, Y., Sievwright, R. H., and Hollings, P. (2020). Multi-stage arc magma evolution recorded by apatite in volcanic rocks. *Geology* 48 (4), 323–327. doi:10.1130/g46998.1
- Palma, G., Barra, F., Reich, M., Valencia, V., Simon, A. C., Vervoort, J., et al. (2019). Halogens, trace element concentrations, and Sr-Nd isotopes in apatite from iron oxide-apatite (IOA) deposits in the Chilean iron belt: Evidence for magmatic and hydrothermal stages of mineralization. *Geochimica Cosmochimica Acta* 246, 515–540. doi:10.1016/j.gca.2018.12.019
- Pan, L. C., Hu, R. Z., Oyebamiji, A., Wu, H. Y., Li, J. W., and Li, J. X. (2021). Contrasting magma compositions between Cu and Au mineralized granodiorite intrusions in the Tongling ore district in South China using apatite chemical composition and Sr-Nd isotopes. *Am. Mineralogist J. Earth Planet. Mater.* 106 (12), 1873–1889. doi:10.2138/am-2021-7497
- Pan, L. C., Hu, R. Z., Wang, X. S., Bi, X. W., Zhu, J. J., and Li, C. (2016). Apatite trace element and halogen compositions as petrogenetic-metallogenic indicators: Examples from four granite plutons in the Sanjiang region, SW China. *Lithos* 254, 118–130. doi:10.1016/j.lithos.2016.03.010

Publisher's note

All claims expressed in this article are solely those of the authors and do not necessarily represent those of their affiliated organizations, or those of the publisher, the editors, and the reviewers. Any product that may be evaluated in this article, or claim that may be made by its manufacturer, is not guaranteed or endorsed by the publisher.

Supplementary material

The Supplementary Material for this article can be found online at: <https://www.frontiersin.org/articles/10.3389/feart.2023.1162994/full#supplementary-material>

SUPPLEMENTARY TABLE S1

Apatite major and trace element compositions with calculated apatite ΣREE , Eu/Eu*, Ce/Ce*, and atoms per formula unit (apfu) values of the Kalmakyr porphyry Cu–Au deposit, Uzbekistan.

SUPPLEMENTARY TABLE S2

Compiled apatite Eu/Eu*, Ce/Ce*, La/Yb, and Sr/Y ratios for ore-bearing and ore-barren intrusions of porphyry deposits.

SUPPLEMENTARY TABLE S3

Compiled apatite SO₃, Cl, F, and F/Cl ratios of porphyry deposits.

- Pan, Y., and Fleet, M. E. (2002). Compositions of the apatite-group minerals: Substitution mechanisms and controlling factors. *Rev. Mineralogy Geochem.* 48 (1), 13–49. doi:10.2138/rmg.2002.48.2
- Parat, F., Holtz, F., and Klügel, A. (2011). S-Rich apatite-hosted glass inclusions in xenoliths from La Palma: Constraints on the volatile partitioning in evolved alkaline magmas. *Contributions Mineralogy Petrology* 162, 463–478. doi:10.1007/s00410-011-0606-7
- Piccoli, P. M., and Candela, P. A. (2002). Apatite in igneous systems. *Rev. Mineralogy Geochem.* 48 (1), 255–292. doi:10.2138/rmg.2002.48.6
- Qin, J., Huang, F., Zhong, S., Wang, D., and Seltmann, R. (2022). Unraveling evolution histories of large hydrothermal systems via garnet U-Pb dating, sulfide trace element and isotopic analyses: A case study of shuikoushan polymetallic ore field, south China. *South China. Ore Geol. Rev.* 149, 105063. doi:10.1016/j.oregeorev.2022.105063
- Qu, P., Li, N. B., Niu, H. C., Shan, Q., Weng, Q., and Zhao, X. C. (2021). Difference in the nature of ore-forming magma between the Mesozoic porphyry Cu-Mo and Mo deposits in NE China: Records from apatite and zircon geochemistry. *Ore Geol. Rev.* 135, 104218. doi:10.1016/j.oregeorev.2021.104218
- Qu, P., Li, N. B., Niu, H. C., Yang, W. B., Shan, Q., and Zhang, Z. Y. (2019). Zircon and apatite as tools to monitor the evolution of fractionated I-type granites from the central Great Xing'an Range, NE China. *Lithos. Lithos* 348, 105207. doi:10.1016/j.lithos.2019.105207
- Richards, J. P. (2011). High Sr/Y arc magmas and porphyry Cu±Mo±Au deposits: Just add water. *Econ. Geol.* 106 (7), 1075–1081. doi:10.2113/econgeo.106.7.1075
- Richards, J. P., López, G. P., Zhu, J. J., Creaser, R. A., Locock, A. J., and Mumin, A. H. (2017). Contrasting tectonic settings and sulfur contents of magmas associated with Cretaceous porphyry Cu±Mo±Au and intrusion-related iron oxide Cu-Au deposits in northern Chile. *Econ. Geol.* 112 (2), 295–318. doi:10.2113/econgeo.112.2.295
- Seltmann, R., Konopelko, D., Biske, G., Divaev, F., and Sergeev, S. (2011). Hercynian post-collisional magmatism in the context of Paleozoic magmatic evolution of the Tien Shan orogenic belt. *J. Asian Earth Sci.* 42 (5), 821–838. doi:10.1016/j.jseas.2010.08.016
- Seltmann, R., Porter, T. M., and Pirajno, F. (2014). Geodynamics and metallogeny of the central Eurasian porphyry and related epithermal mineral systems: A review. *J. Asian Earth Sci.* 79, 810–841. doi:10.1016/j.jseas.2013.03.030
- Sha, L. K., and Chappell, B. W. (1999). Apatite chemical composition, determined by electron microprobe and laser-ablation inductively coupled plasma mass spectrometry, as a probe into granite petrogenesis. *Geochimica Cosmochimica Acta* 63 (22), 3861–3881. doi:10.1016/s0016-7037(99)00210-0
- Sillitoe, R. H. (2010). Porphyry copper systems. *Econ. Geol.* 105 (1), 3–41. doi:10.2113/econgeo.105.1.3
- Stock, M. J., Humphreys, M. C., Smith, V. C., Isaia, R., and Pyle, D. M. (2016). Late-stage volatile saturation as a potential trigger for explosive volcanic eruptions. *Nat. Geosci.* 9 (3), 249–254. doi:10.1038/ngeo2639
- Sun, S. S., and McDonough, W. F. (1989). Chemical and isotopic systematics of oceanic basalts: Implications for mantle composition and processes. *Geol. Soc. Lond. Spec. Publ.* 42 (1), 313–345. doi:10.1144/gsl.sp.1989.042.01.19
- Tang, H., Deng, Z., Zhong, S., Meng, G., Wang, Z., Yuan, L., et al. (2023). Geochemistry and Sr–Nd–Hf–O isotopes of ore-bearing plutons from the Yundukala Au–Cu–Co deposit, East Junggar, Xinjiang, Northwest China: Implications for petrogenesis and tectonic setting. *Ore Geol. Rev.* 153, 105274. doi:10.1016/j.oregeorev.2022.105274
- Turamuratov, I. B., Isokov, M. U., Hodjaev, N. T., Abduazimova, Z. M., Zimalina, V. Y., Tsoy, V. D., et al. (2011). Atlas of ore deposits models of Uzbekistan. *State Comm. Repub. Uzbekistan Geol. Mineral Resour. Sci. Res. Inst. Mineral Resour. Tashkent*, 1–100.
- Xing, K., Shu, Q., and Lentz, D. R. (2021). Constraints on the formation of the giant Dabeishan porphyry Mo deposit (NE China) from whole-rock and accessory mineral geochemistry. *J. Petrology* 62 (4), egab018. doi:10.1093/petrology/egab018
- Xing, K., Shu, Q., Lentz, D. R., and Wang, F. (2020). Zircon and apatite geochemical constraints on the formation of the Huojihe porphyry Mo deposit in the Lesser Xing'an Range, NE China. *Am. Mineralogist J. Earth Planet. Mater.* 105 (3), 382–396. doi:10.2138/am-2020-7226
- Xu, B., Hou, Z. Q., Griffin, W. L., Lu, Y., Belousova, E., Xu, J. F., et al. (2021). Recycled volatiles determine fertility of porphyry deposits in collisional settings. *Am. Mineralogist J. Earth Planet. Mater.* 106 (4), 656–661. doi:10.2138/am-2021-7714
- Yakubchuk, A., Cole, A., Seltmann, R., and Shatov, V. (2002). Tectonic setting, characteristics, and regional exploration criteria for gold mineralization in the altdid orogenic collage: The tien Shan province as a key example. *Soc. Econ. Geol. -Special Publ.* 9, 177–202. doi:10.5382/SP.09.09
- Yang, H. H., Wang, Q., Li, Y. B., Lin, B., Song, Y., Wang, Y. Y., et al. (2022). Geology and mineralization of the tiegelongnan supergiant porphyry-epithermal Cu (Au, Ag) deposit (10 Mt) in Western Tibet, China: A review. *China Geol.* 5 (1), 136–159. doi:10.1016/S2096-5192(22)00091-X
- Yardley, B. W. D. (2005). 100th anniversary special paper: Metal concentrations in crustal fluids and their relationship to ore formation. *Econ. Geol.* 100, 613–632. doi:10.2113/gsecongeo.100.4.613
- Zajacz, Z., Candela, P. A., Piccoli, P. M., Wälle, M., and Sanchez-Valle, C. (2012). Gold and copper in volatile saturated mafic to intermediate magmas: Solubilities, partitioning, and implications for ore deposit formation. *Geochimica Cosmochimica Acta* 91, 140–159. doi:10.1016/j.gca.2012.05.033
- Zhao, X. B., Xue, C. J., Chi, G. X., Mo, X. X., Nurtaev, B., and Zhang, G. Z. (2017). Zircon and molybdenite geochronology and geochemistry of the Kalmakyr porphyry Cu–Au deposit, Almalyk district, Uzbekistan: Implications for mineralization processes. *Ore Geology Reviews. Ore Geol. Rev.* 86, 807–824. doi:10.1016/j.oregeorev.2017.04.008
- Zhao, X. B., Xue, C. J., Chi, G. X., Pak, N., and Zu, B. (2015). Re–Os pyrite and U–Pb zircon geochronology from the Taldybulak Levoberezhny gold deposit: Insight for Cambrian metallogeny of the Kyrgyz northern Tien Shan. *Ore Geol. Rev.* 67, 78–89. doi:10.1016/j.oregeorev.2014.12.002
- Zhao, X. B., Xue, C. J., Zu, B., Seltmann, R., Chi, G. X., Dolgoplova, A., et al. (2022). Geology and genesis of the unkurtash intrusion-related gold deposit, tien Shan, Kyrgyzstan. *Econ. Geol.* 117, 1073–1103. doi:10.5382/econgeo.4918
- Zhong, S., Feng, C., Seltmann, R., Li, D., and Dai, Z. (2018a). Geochemical contrasts between late triassic ore-bearing and barren intrusions in the weibao Cu–Pb–Zn deposit, east kunlun mountains, NW China: Constraints from accessory minerals (zircon and apatite). *Mineralium Deposita. Min. Depos.* 53, 855–870. doi:10.1007/s00126-017-0787-8
- Zhong, S., Feng, C., Seltmann, R., Li, D., and Qu, H. (2018b). Can magmatic zircon be distinguished from hydrothermal zircon by trace element composition? The effect of mineral inclusions on zircon trace element composition. *Lithos* 314–315, 646–657. doi:10.1016/j.lithos.2018.06.029
- Zhong, S., Li, S., Feng, C., Gao, Y., Qu, H., Seltmann, R., et al. (2021a). Geochronology and geochemistry of mineralized and barren intrusive rocks in the yemaquan polymetallic skarn deposit, northern qinghai-tibet plateau: A zircon perspective. *Ore Geol. Rev.* 139, 104560. doi:10.1016/j.oregeorev.2021.104560
- Zhong, S., Li, S., Feng, C., Liu, Y., Santosh, M., He, S., et al. (2021b). Porphyry copper and skarn fertility of the northern Qinghai-Tibet Plateau collisional granitoids. *Earth-Science Rev.* 214, 103524. doi:10.1016/j.earscirev.2021.103524
- Zhong, S., Li, S., Seltmann, R., Lai, Z., and Zhou, J. (2021c). The influence of fractionation of REE-enriched minerals on the zircon partition coefficients. *Geosci. Front.* 12, 101094. doi:10.1016/j.gsf.2020.10.002
- Zhong, S., Seltmann, R., Qu, H., and Song, Y. (2019). Characterization of the zircon Ce anomaly for estimation of oxidation state of magmas: A revised Ce/Ce* method. *Mineralogy Petrology* 113, 755–763. doi:10.1007/s00710-019-00682-y
- Zhu, J. J., Hu, R., Bi, X. W., Hollings, P., Zhong, H., Gao, J. F., et al. (2022). Porphyry Cu fertility of eastern Paleo-Tethyan arc magmas: Evidence from zircon and apatite compositions. *Lithos* 424, 106775. doi:10.1016/j.lithos.2022.106775
- Zhu, J. J., Richards, J. P., Rees, C., Creaser, R., DuFrane, S. A., Locock, A., et al. (2018). Elevated magmatic sulfur and chlorine contents in ore-forming magmas at the Red Chris porphyry Cu–Au deposit, northern British Columbia, Canada. *Econ. Geol.* 113 (5), 1047–1075. doi:10.5382/econgeo.2018.4581